RESEARCH ARTICLE

Key Points:
- Magnetic inclusions hosted in silicates are commonly preserved in marine sediments, which is likely due to protection of silicate minerals
- Magnetic mineral inclusions should be considered as an important source of fine-grained magnetic assemblages in marine sediments
- Modeling of the depositional remanent magnetization of magnetic inclusions enables assessment of their paleomagnetic recording capability

Correspondence to:
L. Chang,
liao.chang@pku.edu.cn

Widespread occurrence of silicate-hosted magnetic mineral inclusions in marine sediments and their contribution to paleomagnetic recording

**Liao Chang[1,2]** (iD)**, Andrew P. Roberts[2], David Heslop[2]** (iD)**, Akira Hayashida[3]** (iD)**, Jinhua Li[4], Xiang Zhao[2]** (iD)**, Wei Tian[1], and Qinghua Huang[1]**

[1]Laboratory of Orogenic Belts and Crustal Evolution, School of Earth and Space Sciences, Peking University, Beijing, China, [2]Research School of Earth Sciences, The Australian National University, Canberra, Australia, [3]Department of Environmental Systems Science, Doshisha University, Kyotanabe, Japan, [4]Paleomagnetism and Geochronology Laboratory, Key Laboratory of Earth's Deep Interior, Institute of Geology and Geophysics, Chinese Academy of Sciences, Beijing, China

Abstract Magnetic mineral inclusions occur commonly within other larger mineral phases in igneous rocks and have been demonstrated to preserve important paleomagnetic signals. While the usefulness of magnetic inclusions in igneous rocks has been explored extensively, their presence in sediments has only been speculated upon. The contribution of magnetic inclusions to the magnetization of sediments, therefore, has been elusive. In this study, we use transmission electron microscope (TEM) and magnetic methods to demonstrate the widespread preservation of silicate-hosted magnetic inclusions in marine sedimentary settings. TEM analysis reveals detailed information about the microstructure, chemical composition, grain size, and spatial arrangement of nanoscale magnetic mineral inclusions within larger silicate particles. Our results confirm the expectation that silicate minerals can protect magnetic mineral inclusions from sulfate-reducing diagenesis and increase significantly the preservation potential of iron oxides in inclusions. Magnetic inclusions should, therefore, be considered as a potentially important source of fine-grained magnetic mineral assemblages and represent a missing link in a wide range of sedimentary paleomagnetic and environmental magnetic studies. In addition, we present depositional remanent magnetization (DRM) modeling results to assess the paleomagnetic recording capability of magnetic inclusions. Our simulation demonstrates that deposition of larger silicate particles with magnetic inclusions will be controlled by gravitational and hydrodynamic forces rather than by geomagnetic torques. Thus, even though these large silicates may contain ideal single-domain particles, they cannot contribute meaningfully to paleomagnetic recording. However, smaller (e.g., silt- and clay-sized) silicates with unidirectionally magnetized magnetic inclusions can potentially record a reliable DRM.

1. Introduction

Magnetic iron-titanium oxide mineral inclusions hosted within silicate minerals, e.g., plagioclase ($NaAlSi_3O_8$ to $CaAl_2Si_2O_8$) and clinopyroxene ((Ca, Mg, Fe)$_2Si_2O_6$), occur widely in igneous and metamorphic rocks. The importance of magnetic inclusions for paleomagnetic studies has been recognized since the discovery of ultrafine-grained iron oxides in silicates in the Modipe Gabbro [*Evans et al.*, 1968; *Evans and Wayman*, 1970]. More recently, there has been renewed interest in magnetic mineral inclusions due to the development of single-crystal-based paleomagnetic analysis and the much increased sensitivity of modern cryogenic magnetometers [e.g., *Cottrell and Tarduno*, 1999; *Tarduno et al.*, 2001, 2006, 2010; *Muxworthy and Evans*, 2013; *Sato et al.*, 2015]. Paleomagnetic signals from magnetic mineral inclusions have been investigated extensively to expand knowledge of past magnetic field behavior of the Earth and other bodies within the solar system [e.g., *Tarduno et al.*, 2001, 2010, 2015; *Feinberg et al.*, 2005, 2006; *Lappe et al.*, 2011, 2013; *Muxworthy et al.*, 2013; *Usui et al.*, 2015]. Unlike magnetically unstable multidomain (MD) particles, magnetic mineral inclusions often occur as fine-grained stable single-domain (SSD) or small pseudo-single-domain particles [e.g., *Harrison et al.*, 2002] that are capable of carrying stable remanences over billions of years [*Evans et al.*, 1968]. Moreover, silicate host minerals can protect magnetic inclusions against changes in the local environment that can give rise to chemical alteration. These characteristics make silicate-hosted magnetic mineral inclusions a promising candidate for retaining reliable paleomagnetic signals over long geological time scales [e.g., *Tarduno et al.*, 2006, 2010].
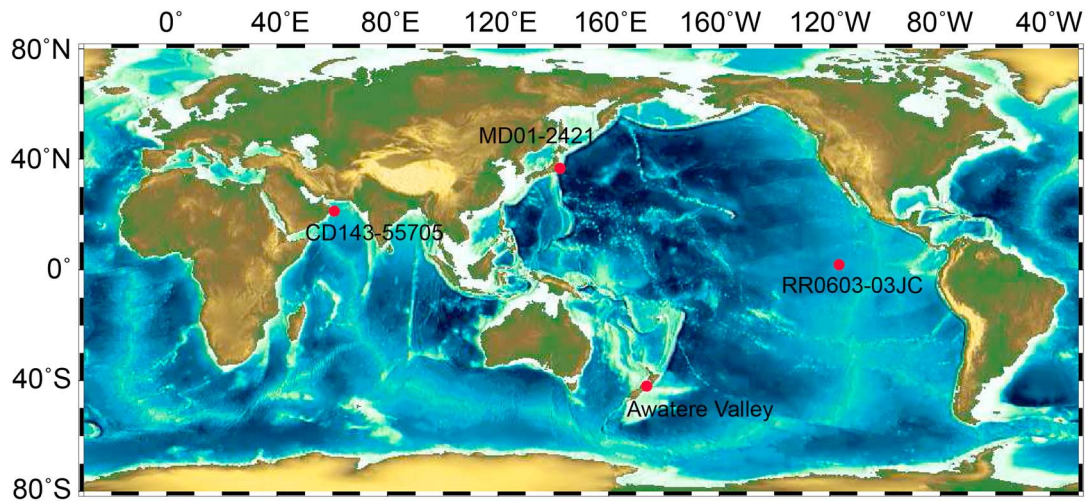
Figure 1. Locations of marine sediment core MD01-2421 from the North Pacific Ocean off the east coast of Japan; core CD143-055705 on the continental margin of Oman; core RR0603-03JC from the eastern equatorial Pacific Ocean; and marine sediment outcrop from the Lower Awatere Valley, northeastern South Island, New Zealand.

The presence of magnetic mineral inclusions in igneous rocks and their important contributions to paleomagnetic records are well established. But knowledge of the presence of magnetic inclusions within detrital particles in sediments and understanding their contribution to sedimentary magnetic signals have been elusive. In this study, we investigated marine sediment samples to search for magnetic mineral inclusions using transmission electron microscope (TEM) and magnetic analyses. We also modeled the depositional remanent magnetization (DRM) of magnetic inclusions to assess their paleomagnetic recording capability. Potential implications of magnetic inclusions for sedimentary paleomagnetic studies are discussed.

2. Materials and Methods

Marine sediment samples from a range of deep-sea sediment cores and sediment outcrops were investigated in this study (Figure 1). Core MD01-2421 (36°01.4′N, 141°46.8′E; 2224 m water depth; 45.82 m long) was recovered from the North Pacific Ocean ~100 km offshore of central Japan [*Oba et al.*, 2006; *Chang et al.*, 2016b]. Sediments in this core are homogenous olive-gray silty clays with calcareous and siliceous microfossils, with high total organic carbon (TOC) content (0.5–2.1 wt % [*Ueshima et al.*, 2006]). Sample "MD01-2421-7-110" from a depth of 110 cm in core section 7 (at a depth of 10.06 m) was analyzed. The studied sample was selected from bulk sediment with no evident disseminated volcanic ash. Core CD143-55705 (22°22.4′N, 60°08.0′E; 2193 m water depth; 10.63 m long) was recovered on the continental margin of Oman, northwestern Arabian Sea [*Rowan et al.*, 2009]. The recovered sediments are homogeneous, light green-brown to gray-green hemipelagic clays, and are high in TOC (1–2%) [*Rowan et al.*, 2009]. Sample "CD143-55705-7-82" from a depth of 82 cm in core section 7 (at 7.49 m depth) was analyzed. Central equatorial Pacific Ocean sediment core RR0603-03JC (2°33′N, 117°55′E; 4195 m water depth) was recovered during the AMAT03 site survey cruise for Integrated Ocean Drilling Program Proposal 626. The lithology of this core is mainly diatom nannofossil ooze. The studied sample "RR0603-03JC-2-60" is from a depth of 60 cm in core section 2 (at 1.04 m depth). Dust may be an important component of the studied samples from the equatorial Pacific Ocean and Arabian Sea. Marine sediment samples (magnetic separate sample "BL37,38,39" and bulk sediment sample "BR49D" that are close to each other stratigraphically) were collected from tectonically uplifted upper Miocene marine sediments exposed in Blind River, Lower Awatere Valley, northeastern South Island, New Zealand [*Roberts and Turner*, 1993]. The succession contains siliciclastic marine sediments of the Awatere Group and is probably derived from greywacke basement rocks and igneous sources in central Marlborough. Key information for the studied samples is summarized in Table 1.

Hysteresis parameters (Table 1) and first-order reversal curve (FORC) measurements were made with a MicroMag vibrating sample magnetometer (model 3900) at the Australian National University (ANU). FORC measurements [*Roberts et al.*, 2000, 2014] were made with a field step of 1.5 mT, maximum applied fields

Table 1. Sample Information and Magnetic Hysteresis Parameters for the Studied Samples

Sample	Location	Water Depth (m)	Core Section	Interval (cm)	Diagenetic zone[c]	B_c (mT)	B_{cr} (mT)	M_{rs}/M_s	B_{cr}/B_c	Domain states
MD01-2421-7-110	North Pacific	2224	7	110–111	Sulfidic	26.3	63	0.289	2.40	SSD
CD143-55705-7-82	Arabian Sea	2193	7	82–83	Sulfidic	14.3	40	0.273	2.80	SSD & trace SP?
RR0603-03JC-2-60[a]	Central Pacific	4195	2	60–62	Ferruginous	17.8	31	0.422	1.74	SSD
BL37,38,39[b]	New Zealand	Outcrop	Lower Awatere Valley		Sulfidic	25.6	52	0.313	2.03	SSD & trace SP?
BR49D	New Zealand	Outcrop	Lower Awatere Valley		Sulfidic	7.0	34	0.292	4.86	SSD & trace MD

[a]Sample "RR0603-03JC-2-60" also contains significant concentrations of biogenic magnetite.
[b]Sample "BL37,38,39" is a magnetic separate studied by *Roberts and Turner* [1993]. All other samples are bulk sediments.
[c]Diagenetic zones are named following the terminology used by *Roberts* [2015].

of 1 T, and averaging times of 200–400 ms. For some magnetically weak samples, we followed the protocol of *Zhao et al.* [2015], in which 120–160 FORCs with irregular measurement grids were measured with averaging times of 200–400 ms. FORC data were processed using the software package of *Zhao et al.* [2015]. No data pretreatments, i.e., removal of first-point artifact and subtraction of lower branch [*Egli*, 2013], were applied. Low-temperature (LT) magnetic properties were measured with a Quantum Design Magnetic Property Measurement System (MPMS; model XL7) at ANU. For warming of a saturation isothermal remanent magnetization (SIRM), samples were first cooled to 10 K in either zero field (zero-field cooled (ZFC)) or in a 5 T field (field-cooled (FC)). At 10 K, a 5 T field was applied and was then switched off to impart a LT SIRM, and the MPMS magnet was reset. ZFC and FC curves were measured during zero-field warming in sweep mode at 5 K/min.

Magnetic minerals were separated from bulk sediments following *Chang et al.* [2012] using a Frantz isodynamic magnetic separator. TEM observations were carried out with a JEOL 2100 F field emission (FE) TEM and a Philips CM300 TEM at the Centre for Advanced Microscopy (CAM), ANU, and with a JEOL 2100 TEM at the Institute of Geology and Geophysics, Chinese Academy of Sciences (CAS). The JEOL 2100 F at CAM is equipped with a FE gun and scanning transmission electron microscope (STEM) detectors and is operated at 200 kV. STEM observations were performed in the high-angle annular darkfield (HAADF) mode. Energy-dispersive X-ray spectroscopy (EDS) analysis was performed using a silicon drift detector with an ultrathin Be window. EDS maps were acquired in the STEM HAADF mode, with a focused electron beam of a few nanometers. The Philips CM300 TEM at CAM is equipped with an EDAS Phoenix retractable X-ray detector and a Gatan CCD camera and is operated at 300 kV. The JEOL 2100 TEM at CAS was operated at 200 kV.

To model DRM, magnetic and hydrodynamic torques that act on a settling detrital particle were compared to assess the ability of magnetic inclusion-bearing particles to align with the geomagnetic field. Detrital sediment particles that contain inclusions are assumed to be prolate ellipsoids. The aspect ratio (ratio of the semimajor axis to the semiminor axis) of such particles plays a key role in controlling their orientation as they settle through the water column. Spherical particles will experience no shape-induced hydrodynamic torque; however, as the aspect ratio of a particle increases, the hydrodynamic torque also increases and tends to rotate a settling ellipsoid so that its long axis is horizontal. The approximation provided by *Heslop* [2007] was employed to find the maximum hydrodynamic torque, τ_H, that acts on a settling particle with a given volume and aspect ratio. Magnetic nanoinclusions within detrital particles are assumed to be SSD magnetite particles with diameters of 100 nm that are aligned along a single preferred crystallographic direction. To represent the magnetization of the magnetite assemblage, we assume that the particles carry a weak-field thermoremanent magnetization (TRM). *Dunlop* [1990] demonstrated that weak-field TRM in magnetite varies as a function of particle size, with an assemblage of randomly oriented 100 nm particles acquiring a TRM of ~10 kA/m in a 100 μT field. We assume that the TRM intensity is proportional to field strength, so we scale this empirical value for a typical geomagnetic field strength of 50 μT. Finally, we multiply the resulting TRM by a factor of 2 to remove the partial cancelation that occurs over a collection of randomly oriented particles. This process yields an estimated TRM of 10 kA/m for aligned particles in a 50 μT field. Assuming that TRM-bearing crystallographically aligned SSD magnetite particles make up a given volume percentage of the host sediment particle, it is possible to estimate the maximum magnetic torque, τ_M, experienced by a sediment particle as it settles through a water column in an ambient 50 μT field.

3. Results

3.1. Magnetic Properties

Magnetic measurements, including FORC and LT measurements (Figure 2), were made on bulk sediment samples (sister samples of the studied TEM samples) and on magnetic separate sample BL37,38,39 to characterize the constituent magnetic minerals and to constrain results from TEM observations. The FORC diagram for sample MD01-2421-7-110 indicates a dominantly SSD signature with moderate magnetostatic interactions (Figure 2a). LT warming of SIRM reveals a weak double Verwey transition (T_v) signature (Figure 2b) that is indicative of the presence of small amounts of both biogenic and inorganic magnetite [e.g., *Chang et al.*, 2016a], where the more pronounced T_v at ~120 K is mostly likely to be associated with the presence of detrital magnetite. It should be noted that the double T_v signature is not observed commonly for other sediment samples from core MD01-2421 [*Chang et al.*, 2016b]. The FORC diagram for sample RR0603-03JC-2-60 from the central equatorial Pacific Ocean contains a dominant central-ridge signature associated with noninteracting SD particles, superposed on a weak background SD signal with stronger interactions (Figure 2c). LT magnetic measurements for this sample did not reveal a clear T_v signal (Figure 2d). The FORC diagram for sample CD143-55705-7-82 from the Oman continental margin contains a SD component with weak to moderate magnetostatic interactions (Figure 2e). This sample has a pronounced T_v at ~120 K (Figure 2f). Sample BR49D from the Lower Awatere Valley, New Zealand, has two major FORC components: a SD distribution with weak to moderate magnetostatic interactions and a MD component with vertical spreading along the B_u axis at low coercivities (Figure 2g). LT data for this sample reveal a pronounced T_v at ~120 K (Figure 2h). The FORC diagram for magnetic separate sample BL37,38,39, which is from an outcrop close to that from which sample BR49D was taken, contains two major FORC distributions: a SD component with moderate vertical spread and a low-coercivity component (Figure 2i). We plot the coercivity profiles from FORC diagrams (Figure 2j) for the studied samples and compare them with published results for some biogenic magnetite samples [*Roberts et al.*, 2013] and magnetic inclusion-bearing igneous rocks [*Muxworthy and Evans*, 2013; *Usui et al.*, 2015]. The B_c profile for sample MD01-2421-7-110 is broader and extends to larger fields compared to other samples, while profiles for other samples containing magnetic nanoinclusions appear to be similar to those for biogenic magnetite.

### 3.2. TEM Observations of Magnetic Mineral Inclusions from Core MD01-2421
3.2.1. Microstructures and Crystallographic Orientations of Magnetic Mineral Inclusions

TEM analysis of magnetic extracts reveals abundant detrital magnetic particles with variable grain sizes, which are probably from igneous lithic fragments sourced from Japan. Large particles are too thick for electron transmission and appear dark under bright-field TEM observations. We selected thinner edge areas from large particles and small particles for our detailed TEM and TEM-EDS analyses. This approach does not enable observations of nanoparticles that occur deeper within large silicate grains. TEM observations reveal abundant nanosized magnetic mineral inclusions (Figure 3) that were difficult to observe in scanning electron microscope observations. The nanosized magnetic minerals must be embedded within host minerals, rather than being attached to particle surfaces, which were clearly visualized by HAADF-STEM imaging due to their different chemical contrast to host minerals (Figures 3a–3d). The nanoparticle inclusions could also be observed by bright-field TEM imaging in the cases of relatively thin or small host minerals (Figures 3e–3i). In both cases, there is a clear contrast shift under TEM between inclusions and hosts from the edge to interior due to variable inclusion depths within the respective host particles. Observed nanoparticle inclusions have sizes that range from a few nanometers to several hundred nanometers with variable morphologies. We observed three main types of inclusion microstructure: nanoparticle clusters (Figures 3a–3c and 3h), dendrites (Figures 3d–3f), and crystallographically oriented nanoparticles (Figure 3g). The nanoparticle clusters consist of euhedral octahedral, subrounded, and irregularly shaped crystals (Figures 3a–3c and 3h). Many of the nanoparticles are nearly isotropic or are slightly elongated; some of which are closely packed (Figures 3b and 3h). We observed less abundant large magnetic mineral inclusions (i.e., ~1 μm; Figure 3i). The observed dendrites have complex microstructures with variable one-, two-, and three-dimensional structures (Figures 3d–3f). Some nanoparticles are assembled along specific crystallographic directions (double-headed arrows in Figures 4a, 4e, and 4f). It is possible that some of the oriented nanoparticles represent arrested dendritic growth. In contrast, some nanoparticle clusters appear to be more randomly distributed within host crystals (Figures 4h and 4i). We carried out selected area electron diffraction
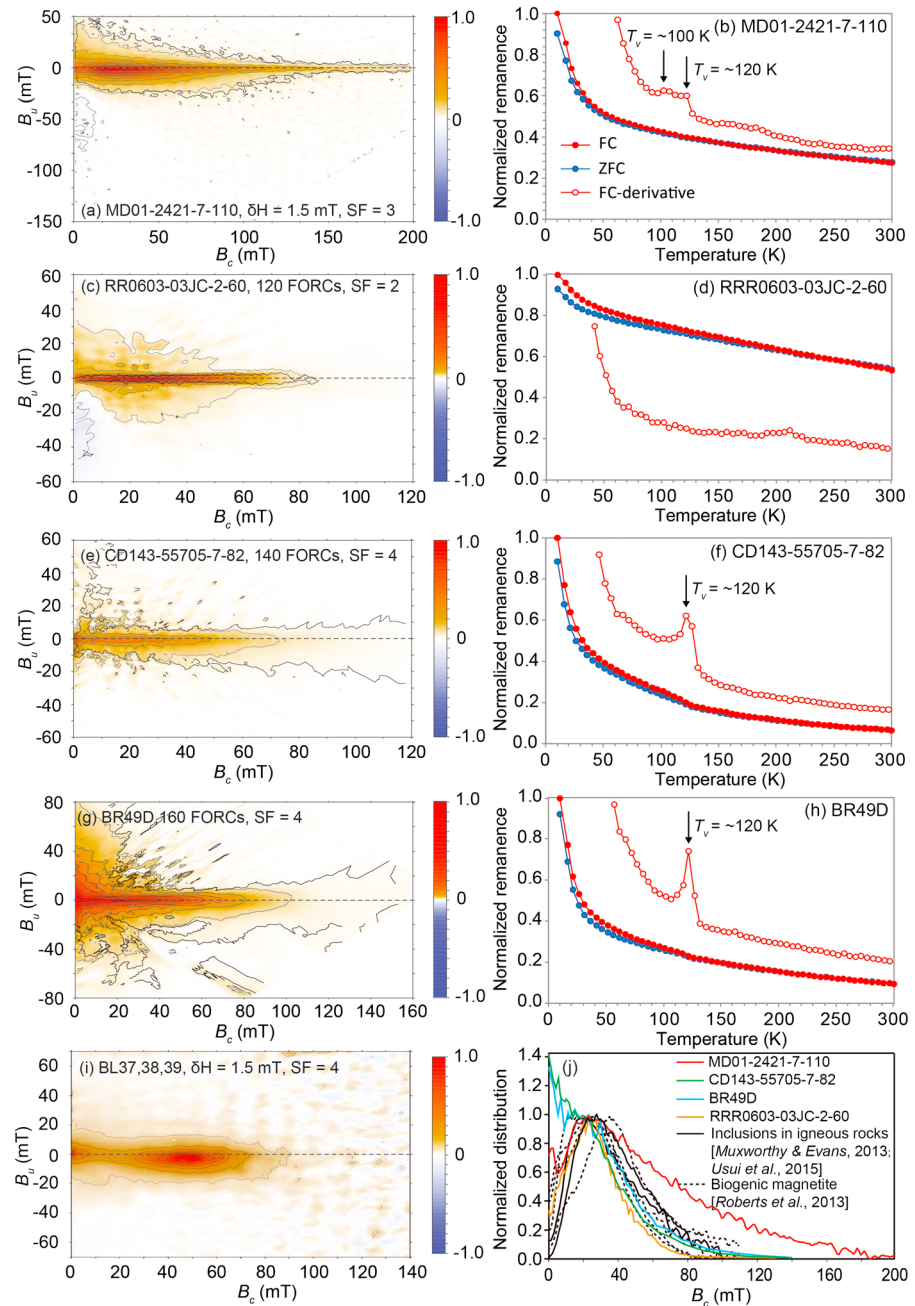
Figure 2. (a, c, e, g, and i) FORC diagrams and (b, d, f, and h) low-temperature SIRM warming curves for (Figures 2a and 2b) sample "MD01-2421-7-110" from the North Pacific Ocean; (Figures 2c and 2d) sample "RR0603-03JC-2-60" from the eastern equatorial Pacific Ocean; (Figures 2e and 2f) sample "CD143-55705-7-82" from the Oman margin, Arabian Sea; and (Figures 2g and 2h) samples "BR49D" and (Figure 2i) "BL37,38,39" from the Lower Awatere Valley, New Zealand. (j) Coercivity distributions (horizontal profiles at $B_u = 0$) extracted from FORC diagrams. Published data are shown in Figure 2j for several marine sediment samples with biogenic magnetite as the dominant magnetic mineral (samples "ODP-738B-4H-6-130," "ODP-738C-11R-1-28," "ODP-689D-8H4-71," and "ODP-690C-9H6-76" [*Roberts et al.*, 2013, Figure 10]) and igneous rocks containing magnetic inclusions (a handpicked sample "B4HP" containing pure pyroxene crystals; Figure 3d [*Muxworthy and Evans*, 2013]) and a handpicked sample containing six plagioclase crystals (Figure 4b [*Usui et al.*, 2015]). "BL37,38,39" is a magnetic separate from *Roberts and Turner* [1993], while all other studied samples are bulk marine sediments. Note that the studied samples also contain other magnetic assemblages in addition to magnetic inclusions (see text for discussion). FORC diagrams in Figures 2c, 2e, and 2g were measured with variable field steps following the protocol of *Zhao et al.* [2015]. All FORC diagrams were processed using the algorithm of *Zhao et al.* [2015]. The thicker black lines correspond to the 0.05 significance level [*Heslop and Roberts*, 2012]. The dashed black lines in the FORC diagrams correspond to the profile of $B_u = 0$.
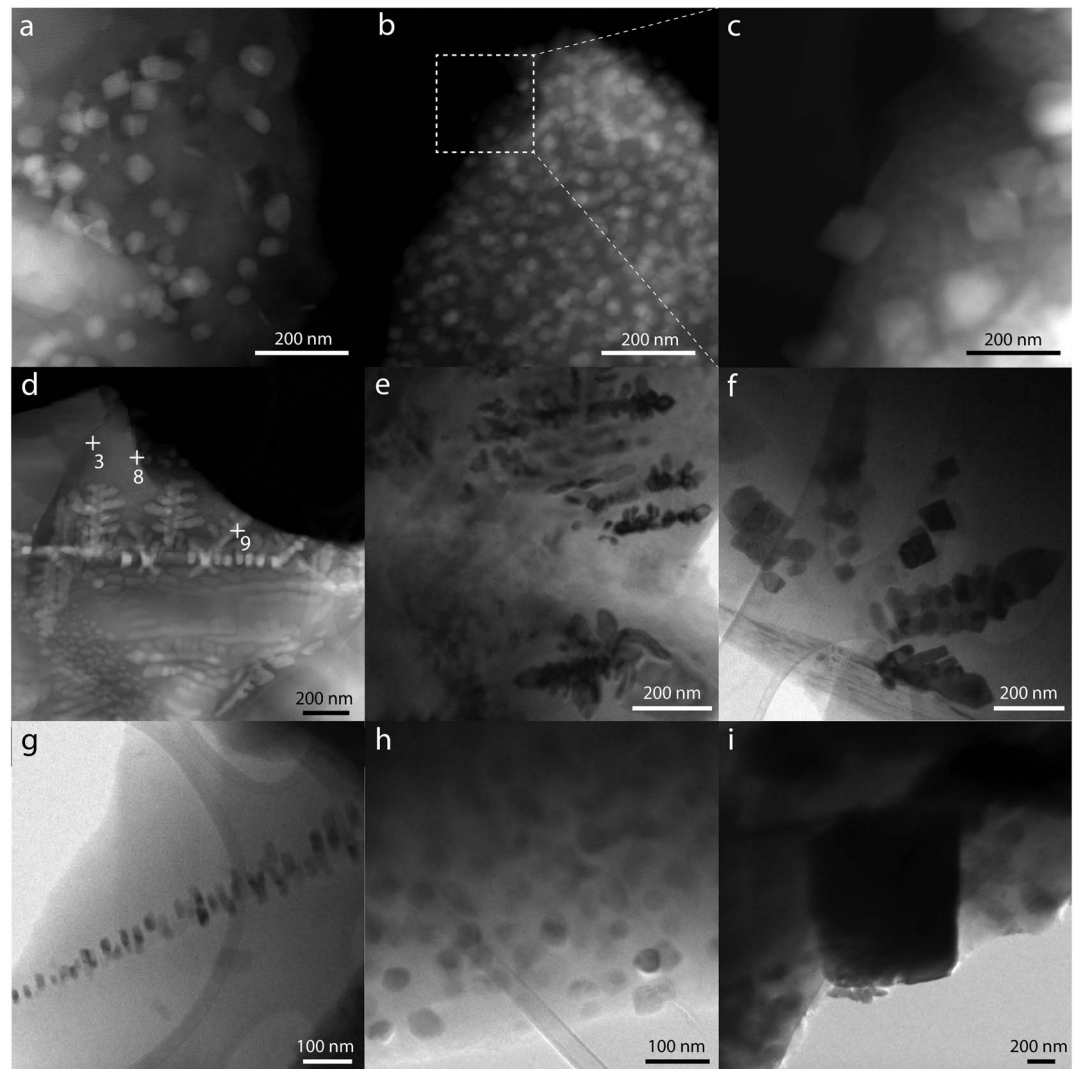
Figure 3. (a–d) STEM and (e–i) bright-field TEM images of microstructures of magnetic nanoparticle inclusions within silicate crystals for sample "MD01-2421-7-110" from the North Pacific Ocean, offshore of central Japan. In the STEM images (Figures 3a–3d), bright particles are mineral inclusions. In the bright-field TEM images (Figures 3e–3i), the mineral inclusions appear dark. Observed morphologies of magnetic mineral inclusions include (Figures 3a–3c and 3h) nanoparticle clusters, (Figures 3d–3f) dendrites, (Figure 3g) crystallographically oriented nanoparticles, and (Figure 3i) a large titanomagnetite inclusion.

(SAED) analysis with the TEM stage tilted at different angles (Figures 4a–4d) to determine the crystallographic orientation of aligned inclusions. During tilting, collective diffraction of nanoparticles (i.e., appearance; Figures 4a–4c, black) and extinction (of nanoparticles; Figure 4d) occurs simultaneously. This behavior confirms a preferential alignment of nanoparticle inclusions within the host crystal, which is further demonstrated by spot-like SAED patterns (insets in Figures 4a–4c). In contrast, some nanoparticle clusters have ring-like diffraction patterns (inset in Figure 4g), which indicate a more random distribution of inclusion orientations.

3.2.2. High-Resolution TEM Analysis of Magnetic Mineral Inclusions and Host Minerals

Further high-resolution TEM (HRTEM) and SAED analyses (Figure 5) indicate that all analyzed magnetic nano-particle inclusions, including clusters and dendrites, have clear lattice fringes (Figures 5d, 5h, 5j, 5l, 5n, and 5p) and strong diffraction patterns (inset in Figure 5b), which indicate good crystallinity. The observed *d*-spacing values and diffraction patterns for the inclusions match well the crystal structure (*Fd*3*m* space group) of magnetite and titanomagnetite. The observed lattice fringes from magnetic mineral inclusions do not reveal
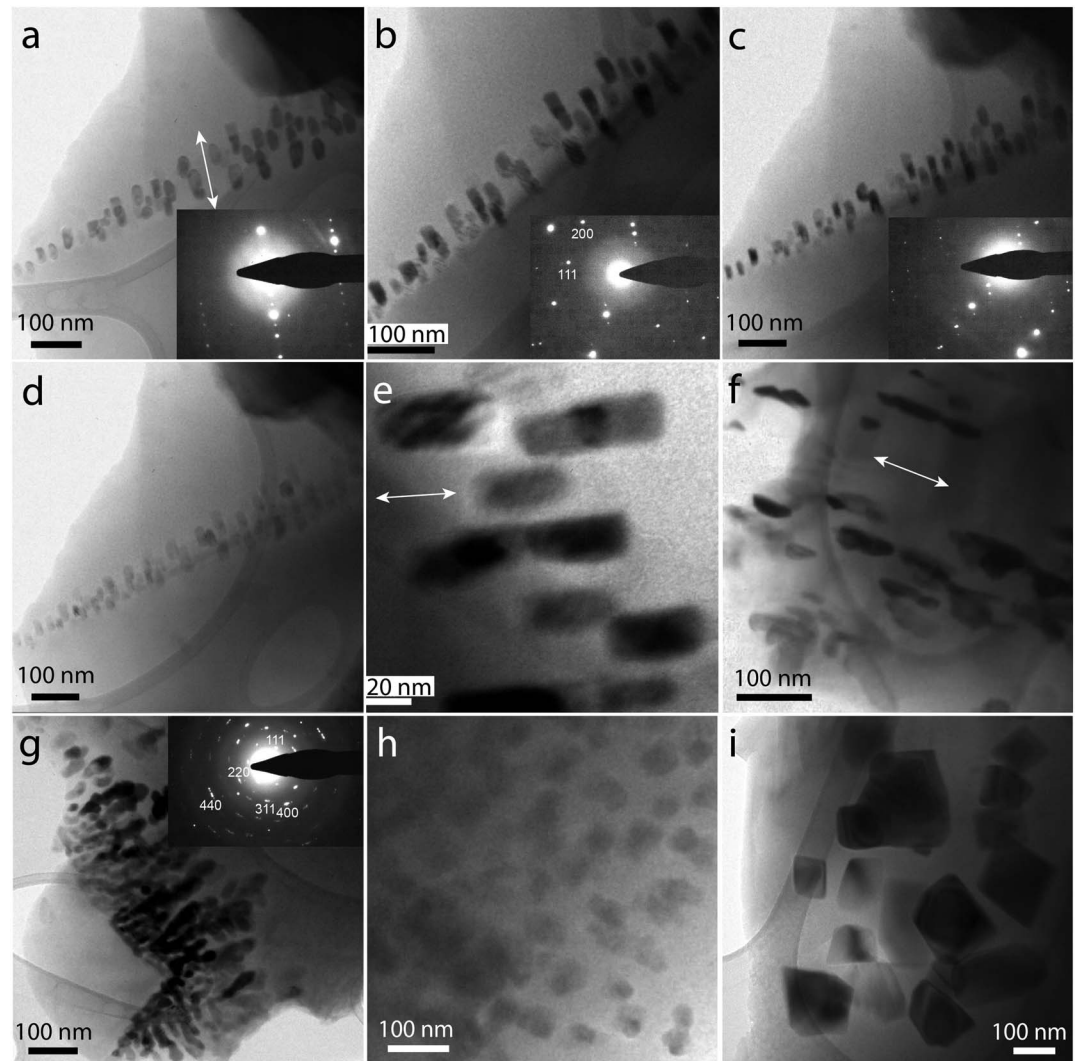
Figure 4. Bright-field TEM images and associated SAED patterns for magnetic mineral inclusions for sample "MD01-2421-7-110." (a–g) The microstructures and electron diffraction patterns indicate that some nanoparticle inclusions have a preferred crystallographic orientation (double headed arrows) within silicate host crystals, (h and i) while other nanoparticles appear to be more randomly oriented (see text for discussion).

signs of crystal defects (Figures 5d, 5h, 5j, 5l, 5n, 5p, 6c, 6d, and 6h). However, we occasionally observed titanomagnetite nanoparticle inclusions with crystal twinning (arrows in Figure 6g). HRTEM and SAED analyses indicate that the host minerals are also crystalline, as evidenced by HRTEM lattice images and SAED patterns (Figures 6e, 6f, and 6i–6l). However, the host minerals generally have weaker diffraction and less clear lattice patterns compared to the inclusions (Figures 6f and 6j). This may be attributed to variable extents of destruction of crystal structures that were observed after a few seconds of electron beam radiation (Figure 6j).

3.2.3. Chemical Compositions

EDS mapping (Figures 7a–7l) and point analyses (Figures 7m–7u) were carried out to determine the chemical composition of inclusions and host crystals. EDS mapping for one area (Figure 7a) indicates that the magnetic mineral inclusions are rich in Fe (Figure 7b) with a much smaller Ti concentration (Figure 7c). The host mineral is rich in O (Figure 7d), and Si (Figure 7e), and also contains a small concentration of Al (Figure 7f) and Ca (data not shown). EDS mapping of another area (Figure 7g) indicates similar characteristics, where the inclusions are Fe rich (Figure 7h), and lacking in Ti (Figure 7i), and the host contains O, Si, and Al (Figures 7j–7l) and Ca (data not shown). EDS spectra of host minerals (Figures 7m, 7p, and 7s) indicate the presence of Si, O,
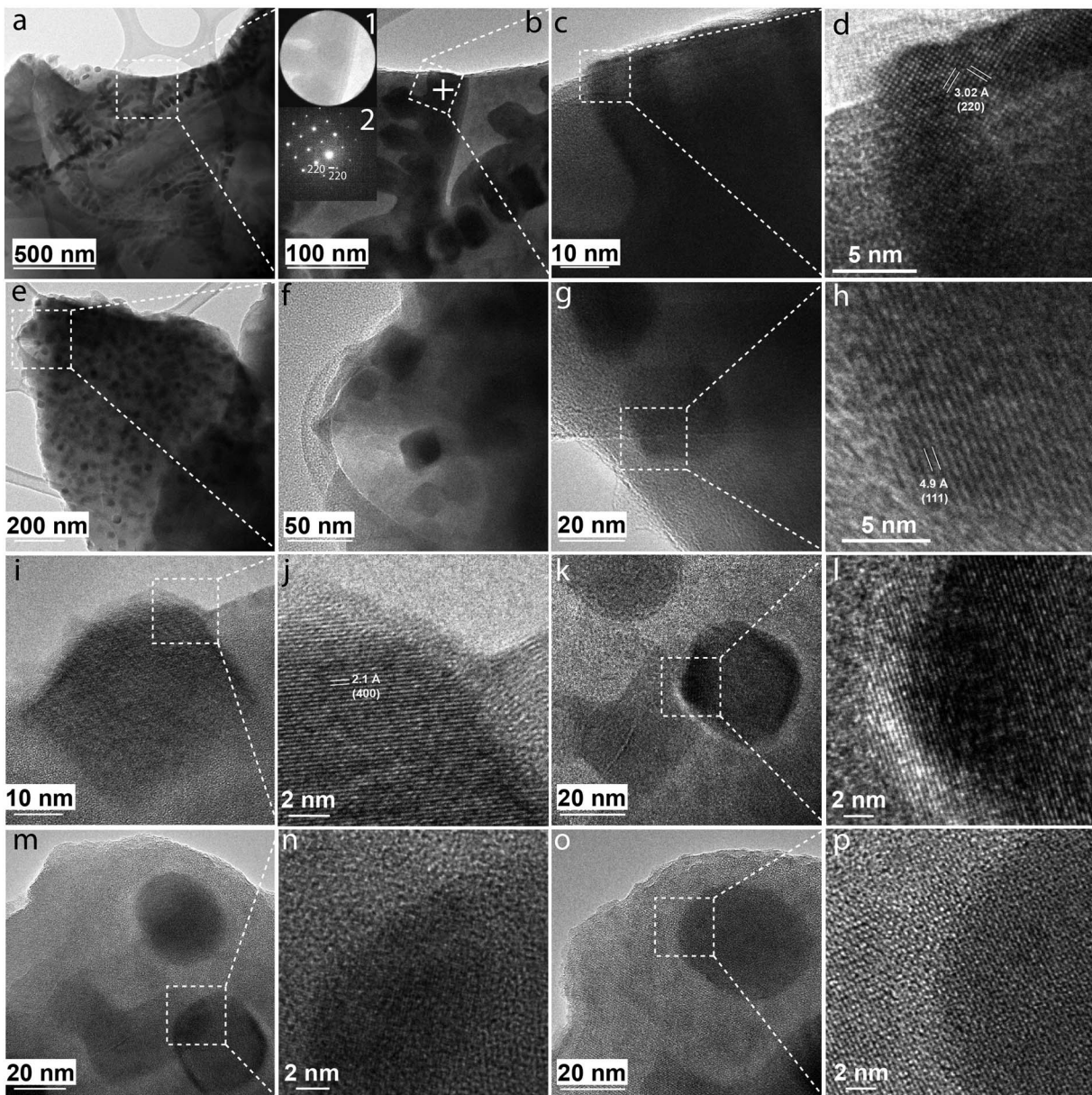
Figure 5. (a–p) Bright-field TEM images at progressively higher magnifications (from left to right for each row of images) that reveal lattice fringes of magnetic mineral inclusions for sample "MD01-2421-7-110." In Figure 5b, the inset image (1) is a bright-field TEM image of the diffracting area (when a diffraction aperture was in the electron beam). The inset image (2) is the corresponding SAED pattern of the area circled in (1). The cross sign in Figure 5b indicates the location of the EDS spot. All analyzed nanoparticles have clear lattice fringes. The host minerals also have clear lattice fringes (Figure 5p). Values of lattice spacings and the corresponding Miller indices (*hkl*) are indicated along the lattice fringes. All measured lattice spacings of mineral inclusions are consistent with those of titanomagnetite or magnetite.

Al, and Ca peaks. EDS spectra of inclusions also contain these elements because they are embedded in host mineral grains, but the EDS spectra of inclusions (Figures 7n, 7o, 7q, 7r, 7t, and 7u) contain much higher concentrations of Fe and minor Ti compared to those of the hosts. The relative intensities of Fe and Ti peaks are variable (ratios are indicated in Figures 7n, 7q, 7r, 7t, and 7u), but Ti contents are small. EDS mapping and point analyses, therefore, consistently indicate that the magnetic mineral inclusions have chemical compositions that are consistent with those in the magnetite-ulvöspinel solid solution series (mainly Ti-poor titanomagnetite). Most of the analyzed host silicate minerals (containing O, Si, Al, and Ca; Figure 7) are plagioclase feldspar. Occasionally, we observed silicate host minerals with O, Si, Ca, Mg, and Fe peaks (data not shown), which are likely to be clinopyroxene.
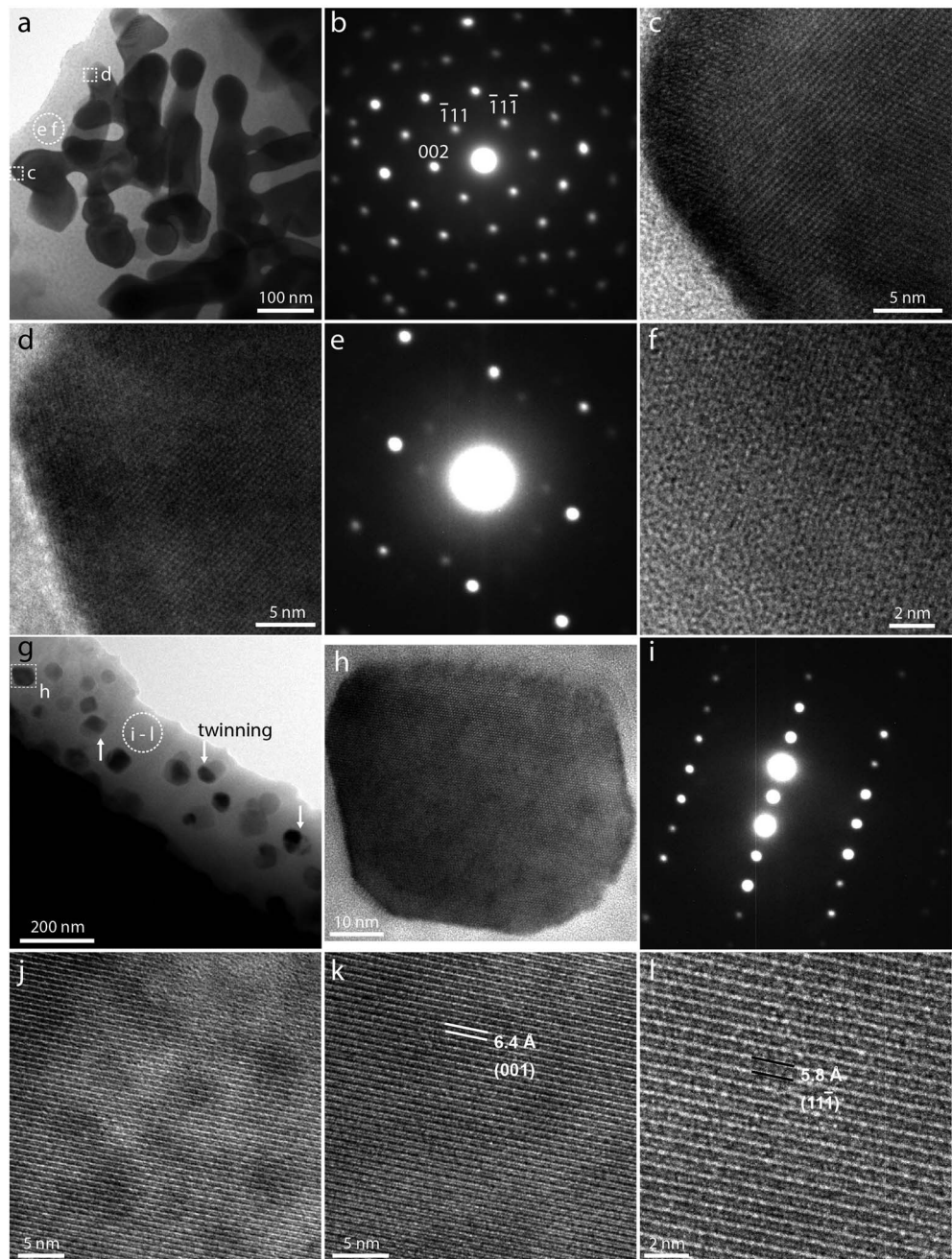
Figure 6. High-resolution TEM and SAED analyses of magnetic mineral inclusions and host minerals for (a–f and g–l) two areas of sample "MD01-2421-7-110." For one area (Figures 6a–6f), images in Figures 6b–6d and 6e and 6f correspond to magnetic mineral inclusions and host minerals, respectively, for areas indicated in Figure 6a. The SAED pattern in Figure 6b is from the whole area in Figure 6a. For another area (Figures 6g–6l), images in Figure 6h and 6i–6l correspond to magnetic mineral inclusions and host minerals, respectively, for areas indicated in Figure 6g. Clear lattice fringes for the inclusions and host minerals are observed. The arrows in Figure 6g indicate the crystal twinning of magnetic nanoparticle inclusions. The mineral inclusions and silicate host minerals are identified to be titanomagnetite and plagioclase, respectively.

3.3. TEM Observations of Marine Sediment Samples from Other Localities

We investigated samples from other localities to test whether magnetic mineral inclusions are commonly present in marine sediments. TEM observations of a marine sediment sample CD143-55705-7-82 from the Oman continental margin reveal the presence of crystallographically orientated small needle-like magnetic minerals within silicates (Figure 8a). This microstructure is consistent with that of exsolved magnetite in
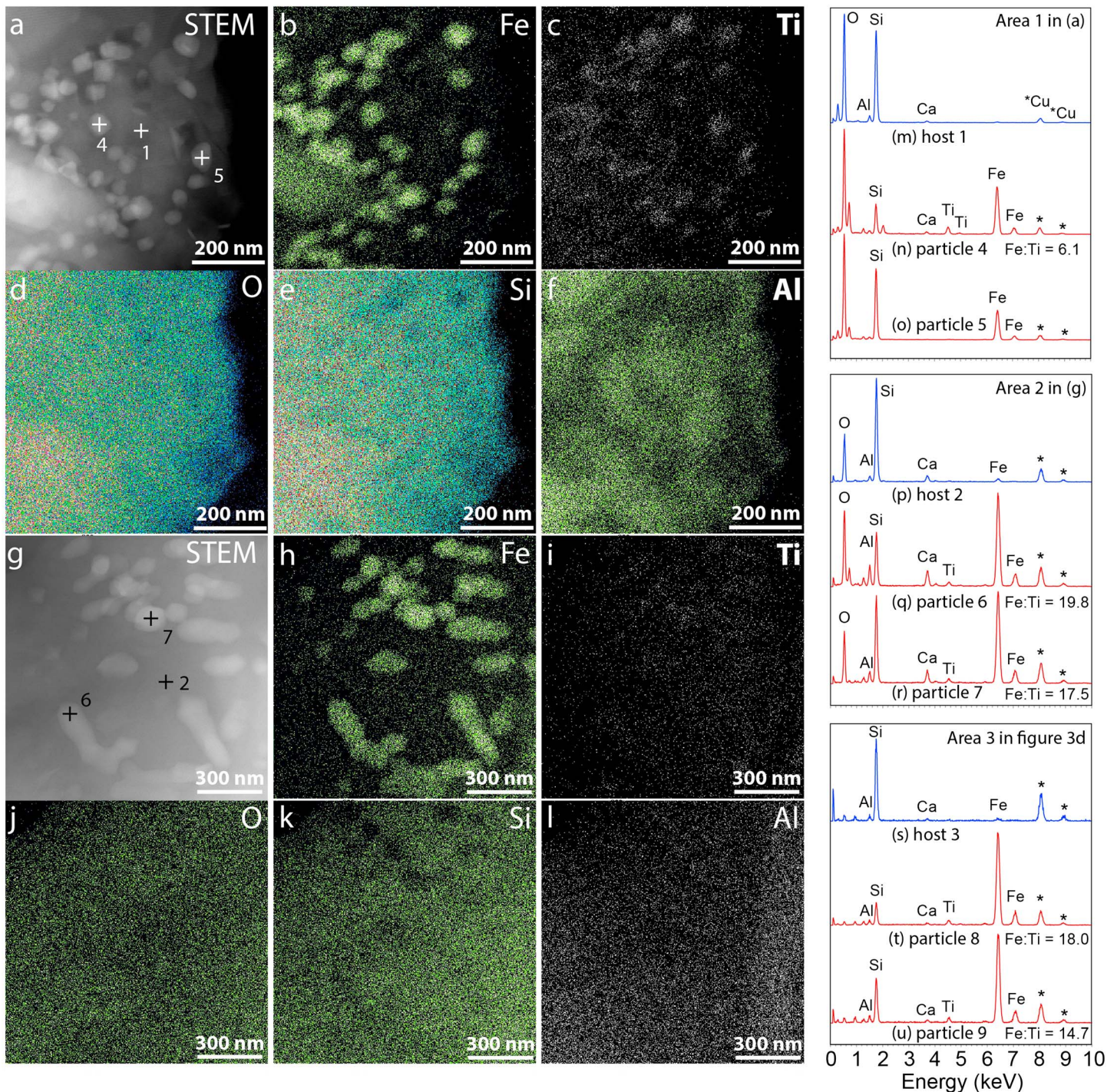
Figure 7. EDS analyses of magnetic mineral inclusions and host minerals. (a and g) STEM images and (b–f and h–l) corresponding elemental maps of two areas within silicate crystals with magnetic nanoparticle inclusions and (m–u) EDS spectra for magnetic nanoparticle inclusions and their host minerals for three analyzed areas in sample "MD01-2421-7-110." The nanoparticle inclusions are rich in Fe but only have small Ti concentrations. The Ti map in Figure 7i is not as clear as that in Figure 7c, which appears to be due to a low Ti content. The EDS spectra of the host mineral contain mainly Si and O, with smaller concentrations of Al and Ca. The host mineral grains (Figures 7a and 7g) are rich in O and Si and contain small concentrations of Ca and Al. The host silicate minerals here are likely to be plagioclase. The nanoparticle inclusions (Figures 7b, 7c, 7e, 7f, 7h, and 7i) are rich in Fe and O and also contain a small Ti peak. The asterisk indicates Cu peaks, which originate from the TEM grid and are present in all spectra. Fe/Ti ratios for titanomagnetite inclusions are indicated for relevant EDS spectra.
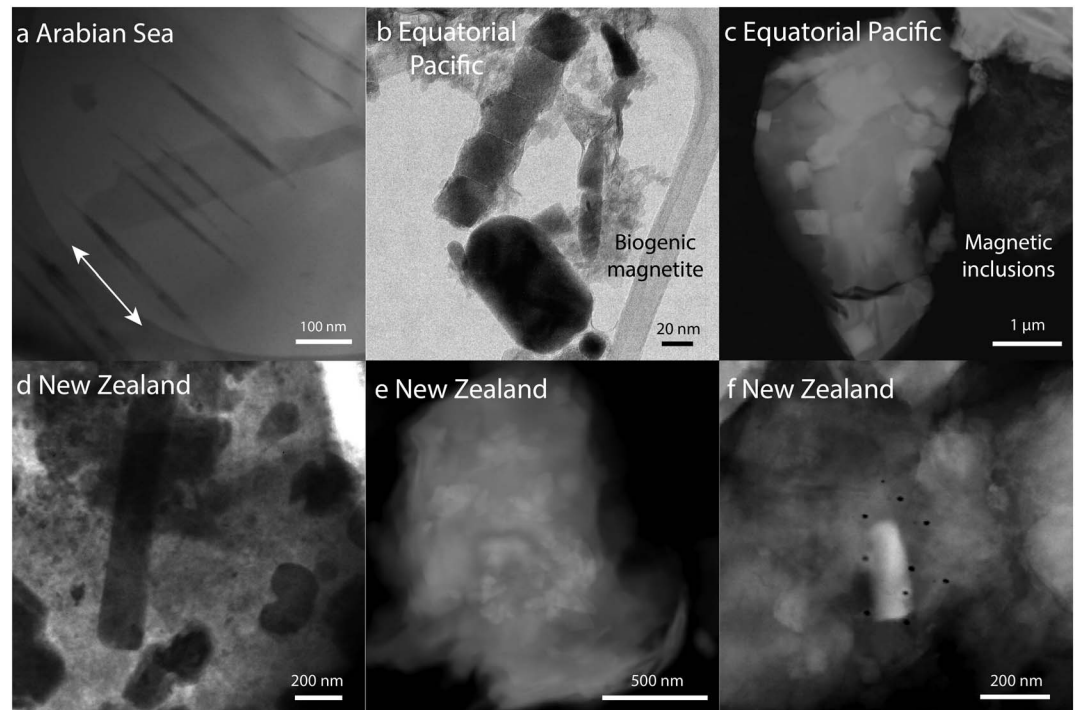
Figure 8. (a) Bright-field TEM image of acicular magnetite inclusions for sample "CD143-55705-7-82" from marine sediment core CD143-55705 from the Oman margin, Arabian Sea. The host mineral is rich in O and Si. The exsolved acicular inclusions appear to have a preferential alignment along their elongation direction (double-headed arrow). (b) A bright-field TEM image of biogenic magnetite crystals and (c) a STEM image of titanomagnetite nanoparticle inclusions hosted in silicates for marine sediment sample "RR0603-03JC-2-60" from eastern equatorial Pacific Ocean core RR0603-03JC. (d) A bright-field TEM and (e and f) STEM images of magnetic mineral inclusions hosted in silicates from magnetic separate sample "BL37,38,39" from the Lower Awatere Valley, New Zealand [*Roberts and Turner*, 1993]. The small black holes in Figure 8f are ablation pits left after EDS point analyses.

igneous rocks. The presence of magnetic mineral inclusions in samples from core CD143-55705 from the Arabian Sea confirms expectations from magnetic analyses (Figures 2e and 2f [*Chang et al.*, 2016a]). TEM analysis on sample RR0603-03JC-2-60 indicates the presence of abundant biogenic magnetite crystals, as evidenced by apparently intact magnetosome chain structures and well-defined magnetosome crystal morphologies (Figure 8b). The TEM results are consistent with a FORC diagram from the same bulk sediment (Figure 2c), which has a strong central-ridge signature [e.g., *Egli et al.*, 2010; *Roberts et al.*, 2012; *Chang et al.*, 2014]. Despite the occurrence of biogenic magnetite in sample RR0603-03JC-2-60, we also observed silicate-hosted titanomagnetite nanoparticles in this sample (Figure 8c). The magnetic separate sample BL37,38,39 from an outcrop in New Zealand contains abundant silicate particles. Detailed TEM analysis of the silicate particles often reveals the presence of Fe-Ti oxide nanocrystals (magnetite or titanomagnetite). Most of the magnetic inclusions appear to be randomly distributed within the silicate hosts (Figure 8d), although possible dendritic titanomagnetite structures are observed (Figure 8e). The host silicate minerals within sample BL37,38,39 often have rough surfaces, with chemical compositions that are consistent with silicates with major Si and O peaks and minor Al, Ca, Na, Fe, or Mg peaks in the EDS spectra.

3.4. Numerical DRM Modeling of Silicate-Hosted Magnetic Inclusions

To make a first-order assessment of the ability of an inclusion-bearing detrital sediment particle to align with the ambient geomagnetic field, we compare τ_H and τ_M for a range of equivalent particle diameters (the diameter of a sphere that has the same volume as the ellipsoid under consideration). To illustrate the relationship between the competing hydrodynamic and magnetic torques, we calculate the aspect ratio for a sediment particle with a given effective diameter and magnetite volume percentage at $\tau_H = \tau_M$ (Figure 9). Our calculation indicates that it would require unrealistically high aspect ratios to achieve $\tau_H = \tau_M$ in smaller particles (i.e., the shape-induced hydrodynamic torque must be increased to infeasibly high levels to achieve
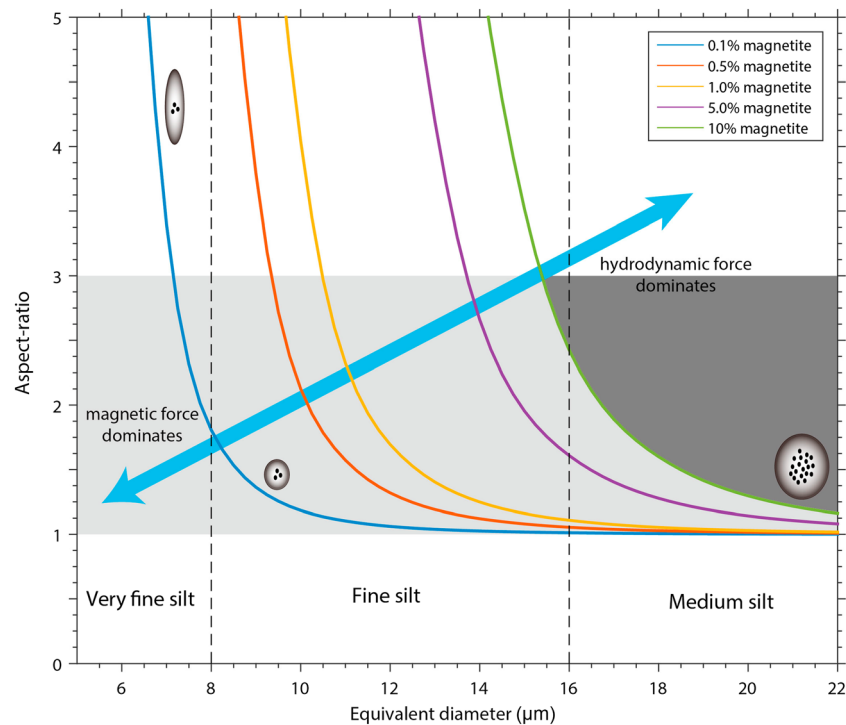
Figure 9. Model results for a DRM carried by magnetic mineral inclusions within silicates. Estimated aspect ratios are shown at which $\tau_H = \tau_M$ for host particles that contain different volume percentages of magnetite nanoparticles (colored lines). To achieve $\tau_H = \tau_M$, smaller particles would require unrealistically high aspect ratios, which indicates that particle orientations are expected to be dominated by magnetic torques. In contrast, larger particles require aspect ratios close to 1, which indicates that the orientation of such particles is expected to be dominated by hydrodynamic torques (see section 2 for details of the numerical simulations). The dashed lines denote the boundaries between very fine, fine, and medium silt. Schematic illustration of prolate ellipsoids alongside the calculated curves represents the modeled silicate particles, which contain embedded magnetite inclusions (black spheres). The light gray area highlights the aspect ratio range of 1–3, in which most detrital particles are expected to fall [*Okada et al.*, 2001]. According to the numerical model, particles (silicates with a volumetric magnetite content of 10%) in the dark gray region should not able to acquire a significant DRM. The arrows indicate the trends of the respective $\tau_H = \tau_M$ lines where the magnetic and hydrodynamic forces balance.

parity with the magnetic torque). Thus, sediment particles in this size range will be dominated by magnetic torques and could contribute to a reliable sedimentary paleomagnetic signal. In contrast, larger sediment particles must have aspect ratios close to 1 to achieve $\tau_H = \tau_M$ (i.e., the shape-induced hydrodynamic torque must be suppressed substantially to achieve parity with the magnetic torque), which is again unrealistic for natural particles. Therefore, larger particles will be dominated by hydrodynamic torques, which will restrict their ability to record reliably the ambient geomagnetic field. The shift from dominance of a magnetic to a hydrodynamic torque in our simple model occurs over a narrow size window within the fine to medium silt size range. The implications of our model results are discussed further below.

4. Discussion

4.1. Widespread Occurrence of Silicate-Hosted Magnetic Inclusions in Marine Sediments

Detrital minerals sourced from continents are important constituents of marine sediments. Our detailed TEM observations indicate that magnetic nanoparticle inclusions are widely present in marine sediments. Magnetic inclusions can even dominate the magnetic signal (Figure 2a) [*Chang et al.*, 2016b]. The observed magnetic mineral microstructures have two main origins due to exsolution and inclusion (see *Tarduno et al.* [2006] for a discussion). Dendrites and crystallographically oriented nanoparticles are exsolved micro-structures in silicates, which form due to phase separation in an originally homogenous solid solution during initial cooling of igneous rocks. Inclusions, such as euhedral crystals, in contrast, form prior to the host silicate

minerals and are incorporated into the host mineral during its subsequent crystallization. Preservation of magnetic mineral inclusions in marine sediments is not surprising. Silicate minerals that host magnetic mineral inclusions occur widely in igneous rocks [e.g., *Evans et al.*, 1968; *Evans and Wayman*, 1970; *Haggerty*, 1991; *Feinberg et al.*, 2006; *Wakabayashi et al.*, 2006], so it is to be expected that such particles will occur as detrital grains in sedimentary strata. However, magnetite is a mixed valence iron oxide mineral that is unstable in both oxidizing and reducing sedimentary environments [*Roberts*, 2015]. In particular, magnetic iron oxide minerals will undergo dissolution during sulfate-reducing diagenesis that results in significant depletion of these minerals and formation of iron sulfide minerals [*Roberts*, 2015]. Unprotected iron oxides, such as coarse-grained magnetic minerals and fine-grained biogenic magnetite, are prone to rapid dissolution in sulfate-reducing marine environments [*Karlin and Levi*, 1983; *Canfield and Berner*, 1987; *Rowan et al.*, 2009; *Chang et al.*, 2016a, 2016b]. The studied sediments from New Zealand and the Japan and Oman margins have undergone extensive sulfidic diagenesis that has removed much of the magnetite signal [*Roberts and Turner*, 1993; *Rowan and Roberts*, 2006; *Rowan et al.*, 2009; *Chang et al.*, 2016a, 2016b]. In contrast, silicate minerals are relatively stable against reductive diagenesis in marine sedimentary environments [*Canfield and Raiswell*, 1991; *Poulton et al.*, 2004; *Roberts*, 2015]. Protection from diagenesis by host silicate crystals will increase the preservation potential of magnetic minerals. Such a protection mechanism is likely to explain the preservation of detrital magnetic minerals in diagenetically altered marine sediments, where magnetite dissolution is expected to be pervasive [*Roberts*, 2015].

4.2. Identification of Magnetic Mineral Inclusions in Sediments

Magnetic mineral inclusions in sediments are important for a wide range of paleomagnetic and environmental magnetic studies. Therefore, robust and efficient methods are needed to identify their presence within sediments. However, this is not straightforward because inclusions are fine-grained (often in the nanometer size range). Also, sediment samples often contain mixed magnetic mineral assemblages. The most robust way to identify magnetic inclusions is by direct TEM observations, as has been demonstrated in this study. But this requires time-consuming experimental work, which makes analysis of large sample sets impossible. We, therefore, explore whether magnetic screening of bulk sediment samples can provide useful indications about the possible presence of magnetic mineral inclusions.

Our detailed TEM and magnetic analyses reveal important properties of magnetic mineral inclusions in sediments that provide clues about their presence. Magnetic mineral inclusions are fine-grained and often have SSD-like magnetic properties (Figure 2). But the grain size distributions of magnetic inclusions can overlap with those of other types of fine particles, such as biogenic magnetite crystals, which can complicate their discrimination. Some magnetic mineral crystals hosted in silicates occur in clusters or as complex dendrites that produce some degree of three-dimensional magnetostatic interactions. Such microstructures differ from those of intact biogenic magnetite chains in sediments, which often produce a noninteracting uniaxial SSD signature [*Egli et al.*, 2010]. Such contrasting properties produce detectable rock magnetic signatures that enable discrimination between these two important types of magnetic minerals in sediments. For example, FORC diagrams with a SSD component and moderate vertical spread (Figures 2a, 2e, and 2g) are a useful indication of the presence of magnetic mineral inclusions [*Lappe et al.*, 2011; *Muxworthy and Evans*, 2013] that contrast with the noninteracting central-ridge FORC signature observed for biogenic magnetite [e.g., *Egli et al.*, 2010; *Roberts et al.*, 2012; *Chang et al.*, 2014]. However, samples that contain dispersed magnetic nanoparticles in silicates can also give rise to FORC signatures with weak magnetostatic interactions [e.g., *Usui et al.*, 2015]. The size distribution of magnetic inclusions is often broad, ranging from just a few nanometers to a few microns (Figures 3–8). Such size distributions can be detected magnetically. For example, decomposition of isothermal remanent magnetization acquisition curves produces a component with large dispersion parameter values (i.e., $> \sim 0.3$) for the studied sample from core MD01-2421. This may also be reflected in the FORC coercivity profiles (Figure 2j). For example, the B_c profile for samples with magnetic inclusions is broad and extends to higher fields, i.e., 200 mT for sample MD01-2421-7-110 from the North Pacific Ocean. This may be because titanomagnetite is magnetically harder than pure magnetite. Low-temperature magnetometry is also useful for detecting magnetic mineral inclusions in sediments (Figure 2). For example, it was demonstrated recently that biogenic and inorganic magnetite in marine sediment samples have two distinct T_v temperatures clustered at ~100 and 120 K, respectively [*Chang et al.*, 2016a]. Thus, combined magnetic analyses, such as a T_v signature at 120 K together with a SSD FORC signature with weak or moderate magnetostatic

interactions, provide a practically useful way to discriminate magnetite inclusions from biogenic magnetite within sediment samples (Figure 2). Nevertheless, definite rock magnetic identification of magnetic mineral inclusions is difficult to achieve because sediment samples often contain mixed magnetic mineral assemblages and also because similar coercivity distributions and magnetostatic interactions can be observed for both lithogenic and biogenic magnetite (Figure 2).

4.3. Implications for Sedimentary Magnetism and Paleomagnetism

Identification of magnetic mineral inclusions within detrital particles has important implications for understanding the magnetization of marine sediments and paleomagnetism. First, our results demonstrate that silicate-hosted magnetic nanoparticles are an important source of fine-grained SSD particles in marine sediments, in addition to biogenic magnetite [e.g., *Roberts et al.*, 2012]. SSD magnetic minerals are important for paleomagnetic studies because they are ideal magnetic recorders that can carry stable remanences over long periods of geological time [*Dunlop and Özdemir*, 1997]. Second, compared to unprotected magnetic mineral particles, silicate-hosted magnetic inclusions have a much higher preservation potential against sulfate-reducing diagenesis. This preservation will have a potentially important influence on environmental magnetic records. For example, an integrated study of marine sediment core MD01-2421 from the continental margin of Japan demonstrates that monsoon-controlled changes in nonsteady state diagenetic conditions can drive preferential dissolution of different populations of magnetic mineral grains. Such diagenetic processes produced a periodically varying sedimentary magnetic pattern throughout the core, where monsoon events gave rise to an enhanced environmental magnetic signal from magnetic inclusions that would otherwise have been destroyed by reductive diagenesis [*Chang et al.*, 2016b]. The possible presence of magnetic nanoinclusions within detrital particles is, therefore, likely to be important for interpreting diagenetically altered marine sediment records in a wide range of settings. Third, igneous formation of silicate-hosted magnetic nanoparticles is related to a range of factors, such as oxygen fugacity, cation content, temperature, and pressure. The transportation pathway of erosional detritus from igneous rocks into marine environments is also sensitive to environmental conditions. Therefore, detection and characterization of silicate-hosted magnetic inclusions preserved in marine sediments could also be useful for tracking geological provenance.

Characterization of silicate-hosted magnetic mineral inclusions is also potentially important for paleomagnetic studies. Significant questions exist about their potential paleomagnetic recording capability. For igneous rocks that contain such magnetic inclusions, how do they acquire a TRM and is the anisotropy of elongated particles important for interpreting paleomagnetic signals? How do magnetostatic interactions among such nanoparticles affect paleomagnetic recording fidelity [e.g., *Feinberg et al.*, 2006]? Our characterization of microstructures of magnetic mineral inclusions and hosts indicate that these are important questions to address when subjecting such materials to paleomagnetic analysis. For example, three-dimensional micromagnetic models can be constructed to simulate the magnetic properties of magnetic mineral inclusions with complex morphologies and their paleomagnetic recording fidelity can be assessed quantitatively [e.g., *Williams et al.*, 2010; *Muxworthy and Evans*, 2013]. Moreover, single plagioclase crystals that contain magnetic mineral inclusions have been used for absolute paleointensity determinations [e.g., *Tarduno et al.*, 2001]. Some of our silicates differ from those documented in prior paleointensity and paleomagnetic studies of single silicate crystals, particularly in the density of inclusions; this may be partially due to selection criteria in those studies that excludes crystals with visible inclusions (at low magnification) that are aimed at avoiding MD magnetic carriers [e.g., *Tarduno et al.*, 2006]. However, the presence of silicates with high inclusion density in our sediments highlights the continued need to test for the possibility of interactions by nanoscale imaging [e.g., *Feinberg et al.*, 2006; *Bono and Tarduno*, 2015], FORC analyses [e.g., *Tarduno and Cottrell*, 2005], and the application of paleointensity selection criteria (the latter can suggest the presence of interactions if natural remanent magnetization/TRM plots are nonlinear).

An important question to consider in relation to sedimentary paleomagnetic recording is how efficiently do magnetic mineral inclusions in silicates produce a DRM in sediments? The large size of some host silicate particles (ranging from microns to hundreds of microns) means that hydrodynamic forces will be important during deposition and that large particles are unlikely to be aligned by a geomagnetic torque (Figure 9). It is, therefore, to be expected that such large particles will contribute to randomization of sedimentary paleomagnetic signals. But how do such particles compare with the particle size distributions of sediments that

are subjected to paleomagnetic investigations? Sandstones are rarely used for paleomagnetic analysis because even if magnetic particles occur in the finest possible sand category (very fine sand), they will have sizes of at least 50 μm. Such magnetic particles will have MD properties that will not enable recording of a stable paleomagnetic signal. Likewise, sand-sized host particles with magnetic nanoinclusions will be dominated by hydrodynamic rather than by magnetic torques and will not record a stable paleomagnetic signal (Figure 9). In contrast, clay-rich sediments (<2 μm) are often considered ideal for paleomagnetic analysis because fine particles are more likely to give rise to stable paleomagnetic recording. However, clay minerals are products of weathering rather than being primary detrital minerals that have been abraded to ultrafine sizes, so that much of the clay size fraction in a sediment will be due to clay minerals. Nevertheless, some part of the clay size fraction of sediments could represent particles that have been abraded to ultrafine sizes.

Windblown sediment particles are likely to have greater roughness than other types of sediments that have been rounded extensively through abrasion in fluvial and other aquatic systems and provide a worthwhile end-member for considering particle aspect ratios and the effects of hydrodynamic versus magnetic torques. *Okada et al.* [2001] analyzed particle shapes for atmospherically transported mineral particles from three Chinese arid regions. These fine silt- to clay-sized detrital mineral particles (0.1 to 6 μm) have irregular shapes as expected, with aspect ratios that are size independent and that range from values of 1 to ~3 (shaded region in Figure 9), with skewed distributions and median aspect ratios of 1.3 to 1.4. Virtually 100% of their analyzed mineral particles have aspect ratios <5. The results of *Okada et al.* [2001] place useful constraints on the region of Figure 9 that is likely to be meaningful for paleomagnetic recording of host particles with magnetic nanoinclusions. From the results of our simple models, it appears that host silicate particles that contain magnetite nanoinclusions should be capable of contributing to sedimentary paleomagnetic records at equivalent particle diameters below 12 μm for 1% magnetite concentrations (Figure 9). The effective diameter of particles that can be aligned by geomagnetic torques will increase for larger magnetite nanoinclusion concentrations.

Following the above arguments, silicate-hosted magnetic inclusions could be important for paleomagnetic recording in silt- and clay-sized sediments. It is unlikely that magnetite-rich host silicates will contribute to the magnetization of medium silts with particle sizes above ~18–20 μm (Figure 9). Sediments always contain a distribution of particle sizes. Size distributions that cross the $\tau_H = \tau_M$ line, which from Figure 9 is likely to occur in silt- and clay-sized sediments, will have some capacity for reliable paleomagnetic recording with considerable partial cancelation due to both particle types. The resulting magnetization will not be efficient, which is consistent with the low efficiency of sedimentary magnetizations [e.g., *Tauxe et al.*, 2006; *Mitra and Tauxe*, 2009; *Heslop et al.*, 2014]. Regardless, the simple model results presented in Figure 9 should be considered a best-case scenario for paleomagnetic recording. Some silicate inclusions will have two or more preferred crystallographic orientations of inclusions [e.g., *Feinberg et al.*, 2006], for which variable extents of magnetic moment cancelation would be expected.

5. Conclusions

TEM observations of magnetic mineral extracts from geographically widely distributed samples confirm the abundant occurrence of magnetic nanoparticle inclusions hosted within silicate crystals in marine sediments. We document variable inclusion morphologies, including isolated nanoparticles (i.e., octahedra, subrounded, and irregular shapes), nanoparticle clusters, and dendrites. EDS analysis indicates that the magnetic mineral inclusions consist of magnetite to titanomagnetite (with low but variable Ti contents), while the hosts are silicate minerals (mostly plagioclase feldspar and clinopyroxene). Some magnetic nanoparticles occur with crystallographically preferred orientations within the host silicates. The inclusion density in some of the silicates isolated here differs from those documented in rock magnetic and paleomagnetic studies [e.g., *Feinberg et al.*, 2005; *Bono and Tarduno*, 2015]; while such particles may have been excluded in prior paleomagnetic and paleointensity studies by the selection criteria used [e.g., *Tarduno et al.*, 2006], they may be magnetically important in sedimentary paleomagnetism. Silicate minerals are relatively stable against diagenetic alteration in sulfate-reducing diagenetic environments, which can, therefore, protect the embedded mineral inclusions from dissolution. Our results demonstrate that silicate-hosted magnetic mineral inclusions are an important source of fine-grained magnetic minerals in sediments and provide important constraints on understanding sedimentary paleomagnetic and environmental magnetic records. The DRM of magnetic

inclusions was modeled to assess their paleomagnetic recording capability. Calculations indicate that deposition of large silicate particles will be controlled by hydrodynamic forces rather than by geomagnetic torques, so that even if large particles may contain ideal SSD inclusions, they are unlikely to contribute meaningfully to paleomagnetic recording. Nevertheless, deposition of smaller silicate particles with magnetic mineral inclusions could give rise to a reliable paleomagnetic record.

References

Bono, R. K., and J. A. Tarduno (2015), A stable Ediacaran Earth recorded by single silicate crystals of the ca. 565 Ma Sept-Îles intrusion, *Geology*, *43*, 131–134, doi:10.1130/G36247.1.

Canfield, D. E., and R. A. Berner (1987), Dissolution and pyritization of magnetite in anoxic marine sediments, *Geochim. Cosmochim. Acta*, *51*, 645–659, doi:10.1016/0016-7037(87)90076-7.

Canfield, D. E., and R. Raiswell (1991), Pyrite formation and fossil preservation, in *Taphonomy: Releasing the Data Locked in the Fossil Record*, edited by P. A. Allison and D. E. G. Briggs, pp. 337–387, Plenum Press, New York.

Chang, L., A. P. Roberts, W. Williams, J. D. Fitz Gerald, J. C. Larrasoaña, L. Jovane, and A. R. Muxworthy (2012), Giant magnetofossils and hyperthermal events, *Earth Planet. Sci. Lett.*, *351–352*, 258–269, doi:10.1016/j.epsl.2012.07.031.

Chang, L., A. P. Roberts, M. Winklhofer, D. Heslop, M. J. Dekkers, W. Krijgsman, J. D. Fitz Gerald, and P. Smith (2014), Magnetic detection and characterization of biogenic magnetic minerals: A comparison of ferromagnetic resonance and first-order reversal curve diagrams, *J. Geophys. Res. Solid Earth*, *119*, 6136–6158, doi:10.1002/2014JB011213.

Chang, L., D. Heslop, A. P. Roberts, D. Rey, and K. J. Mohamed (2016a), Discrimination of biogenic and detrital magnetite through a double Verwey transition temperature, *J. Geophys. Res. Solid Earth*, *121*, 3–14, doi:10.1002/2015JB012485.

Chang, L., et al. (2016b), Asian monsoon modulation of nonsteady state diagenesis in hemipelagic marine sediments offshore of Japan, *Geochem. Geophys. Geosyst.*, *17*, doi:10.1002/2016GC006344.

Cottrell, R. D., and J. A. Tarduno (1999), Geomagnetic paleointensity derived from single plagioclase crystals, *Earth Planet. Sci. Lett.*, *169*, 1–5, doi:10.1016/S0012-821X(99)00068-0.

Dunlop, D. J. (1990), Developments in rock magnetism, *Repts. Progr. Phys.*, *53*, 707–792.

Dunlop, D. J., and Ö. Özdemir (1997), *Rock Magnetism: Fundamentals and Frontiers*, 573 pp., Cambridge Univ. Press, Cambridge, U. K.

Egli, R. (2013), VARIFORC: An optimized protocol for calculating non-regular first-order reversal curve (FORC) diagrams, *Global Planet. Change*, *110*, 302–320, doi:10.1016/j.gloplacha.2013.08.003.

Egli, R., A. P. Chen, M. Winklhofer, K. P. Kodama, and C.-S. Horng (2010), Detection of noninteracting single domain particles using first-order reversal curve diagrams, *Geochem. Geophys. Geosyst.*, *11*, Q01Z11, doi:10.1029/2009GC002916.

Evans, M. E., and M. L. Wayman (1970), Investigation of small magnetic particles by means of electron microscopy, *Earth Planet. Sci. Lett.*, *9*, 365–370.

Evans, M. E., M. W. McElhinny, and A. C. Gifford (1968), Single domain magnetite and high coercivities in a gabbroic intrusion, *Earth Planet. Sci. Lett.*, *4*, 142–146.

Feinberg, J. M., G. R. Scott, P. R. Renne, and H. R. Wenk (2005), Exsolved magnetite inclusions in silicates: Features determining their remanence behavior, *Geology*, *33*, 513–516.

Feinberg, J. M., R. J. Harrison, T. Kasama, R. E. Dunin-Borkowski, G. R. Scott, and P. R. Renne (2006), Effects of internal mineral structures on the magnetic remanence of silicate-hosted titanomagnetite inclusions: An electron holography study, *J. Geophys. Res.*, *111*, B12S15, doi:10.1029/2006JB004498.

Haggerty, S. E. (1991), Oxide mineralogy of the upper mantle, edited by D. H. Lindsley, Oxide Minerals: Petrologic and Magnetic Significance, *Rev. Mineral.*, *25*, 355–416.

Harrison, R. J., R. E. Dunin-Borkowski, and A. Putnis (2002), Direct imaging of nanoscale magnetic interactions in minerals, *Proc. Natl. Acad. Sci. U.S.A.*, *99*, 16,556–16,561.

Heslop, D. (2007), Are hydrodynamic shape effects important when modelling the formation of depositional remanent magnetization?, *Geophys. J. Int.*, *171*, 1029–1035, doi:10.1111/j.1365-246X.2007.03588.x.

Heslop, D., and A. P. Roberts (2012), Estimation of significance levels and confidence intervals for first-order reversal curve distributions, *Geochem. Geophys. Geosyst.*, *13*, Q12Z40, doi:10.1029/2012GC004115.

Heslop, D., A. P. Roberts, and R. Hawkins (2014), A statistical simulation of magnetic particle alignment in sediments, *Geophys. J. Int.*, *197*, 828–837.

Karlin, R., and S. Levi (1983), Diagenesis of magnetic minerals in recent haemipelagic sediments, *Nature*, *303*, 327–330.

Lappe, S.-C. L. L., N. Church, T. Kasama, A. Fanta, G. Bromiley, R. E. Dunin-Borkowski, J. M. Feinberg, S. Russell, and R. J. Harrison (2011), Mineral magnetism of dusty olivine: A credible recorder of pre-accretionary remanence, *Geochem. Geophys. Geosyst.*, *12*, Q12Z35, doi:10.1029/2011GC003811.

Lappe, S.-C. L. L., J. M. Feinberg, A. Muxworthy, and R. J. Harrison (2013), Comparison and calibration of nonheating paleointensity methods: A case study using dusty olivine, *Geochem. Geophys. Geosyst.*, *14*, 2143–2158, doi:10.1002/ggge.20141.

Mitra, R., and L. Tauxe (2009), Full vector model for magnetization in sediments, *Earth Planet. Sci. Lett.*, *286*, 535–545.

Muxworthy, A. R., and M. E. Evans (2013), Micromagnetics and magnetomineralogy of ultrafine magnetite inclusions in the Modipe Gabbro, *Geochem. Geophys. Geosyst.*, *14*, 921–928, doi:10.1029/2012GC004445.

Muxworthy, A. R., M. E. Evans, S. J. Scourfield, and J. G. King (2013), Paleointensity results from the late-Archaean Modipe Gabbro of Botswana, *Geochem. Geophys. Geosyst.*, *14*, 2198–2205, doi:10.1002/ggge.20142.

Oba, T., T. Irino, M. Yamamoto, M. Murayama, A. Takamura, and K. Aoki (2006), Paleoceanographic change off central Japan since the last 144,000 years based on high-resolution oxygen and carbon isotope records, *Global Planet. Change*, *53*, 5–20.

Okada, K., J. Heintzenberg, K. Kai, and Y. Qin (2001), Shape of atmospheric mineral particles collected in three Chinese arid-regions, *Geophys. Res. Lett.*, *28*, 3123–3126, doi:10.1029/2000GL012798.

Poulton, S. W., M. D. Krom, and R. Raiswell (2004), A revised scheme for the reactivity of iron (oxyhydr)oxide minerals towards dissolved sulfide, *Geochim. Cosmochim. Acta*, *68*, 3703–3715.

Roberts, A. P. (2015), Magnetic mineral diagenesis, *Earth-Sci. Rev.*, *151*, 1–47.

Roberts, A. P., and G. M. Turner (1993), Diagenetic formation of ferrimagnetic iron sulphide minerals in rapidly deposited marine sediments, South Island, New Zealand, *Earth Planet. Sci. Lett.*, *115*, 257–273.

Roberts, A. P., C. R. Pike, and K. L. Verosub (2000), First-order reversal curve diagrams: A new tool for characterizing the magnetic properties of natural samples, *J. Geophys. Res.*, *105*, 28,461–28,475, doi:10.1029/2000JB900326.

Roberts, A. P., L. Chang, D. Heslop, F. Florindo, and J. C. Larrasoaña (2012), Searching for single domain magnetite in the "pseudo-single-domain" sedimentary haystack: Implications of biogenic magnetite preservation for sediment magnetism and relative paleointensity determinations, *J. Geophys. Res.*, *117*, B08104, doi:10.1029/2012JB009412.

Roberts, A. P., F. Florindo, L. Chang, D. Heslop, L. Jovane, and J. C. Larrasoaña (2013), Magnetic properties of pelagic marine carbonates, *Earth-Sci. Rev.*, *127*, 111–139.

Roberts, A. P., D. Heslop, X. Zhao, and C. R. Pike (2014), Understanding fine magnetic particle systems through use of first-order reversal curve diagrams, *Rev. Geophys.*, *52*, 557–602, doi:10.1002/2014RG000462.

Rowan, C. J., and A. P. Roberts (2006), Magnetite dissolution, diachronous greigite formation, and magnetizations arising from pyrite oxidation: Unravelling complex magnetizations in Neogene marine sediments from New Zealand, *Earth Planet. Sci. Lett.*, *241*, 119–137.

Rowan, C. J., A. P. Roberts, and T. Broadbent (2009), Reductive diagenesis, magnetite dissolution, greigite growth and paleomagnetic smoothing in marine sediments: A new view, *Earth Planet. Sci. Lett.*, *277*, 223–235.

Sato, M., S. Yamamoto, Y. Yamamoto, Y. Okada, M. Ohno, H. Tsunakawa, and S. Maruyama (2015), Rock-magnetic properties of single zircon crystals sampled from the Tanzawa tonalitic pluton, central Japan, *Earth Planets Space*, *67*, 150, doi:10.1186/s40623-015-0317-9.

Tarduno, J. A., and R. D. Cottrell (2005), Dipole strength and variation of the time-averaged reversing and nonreversing geodynamo based on Thellier analyses of single plagioclase crystals, *J. Geophys. Res.*, *110*, B11101, doi:10.1029/2005JB003970.

Tarduno, J. A., R. D. Cottrell, and A. V. Smirnov (2001), High geomagnetic field intensity during the mid-Cretaceous from Thellier analyses of single plagioclase crystals, *Science*, *291*, 1779–1783, doi:10.1126/science.1057519.

Tarduno, J. A., R. D. Cottrell, and A. V. Smirnov (2006), The paleomagnetism of single silicate crystals: Recording geomagnetic field strength during mixed polarity intervals, superchrons, and inner core growth, *Rev. Geophys.*, *44*, RG1002, doi:10.1029/2005RG000189.

Tarduno, J. A., R. D. Cottrell, M. Watkeys, A. Hofmann, P. V. Doubrovine, E. E. Mamajek, D. Liu, D. G. Sibeck, L. P. Neukirch, and Y. Usui (2010), Geodynamo, solar wind, and magnetopause 3.4 to 3.45 billion years ago, *Science*, *327*, 1238–1240.

Tarduno, J. A., R. D. Cottrell, W. J. Davis, F. Nimmo, and R. K. Bono (2015), A Hadean to Paleoarchean geodynamo recorded by single zircon crystals, *Science*, *349*, 521–524.

Tauxe, L., J. L. Steindorf, and A. Harris (2006), Depositional remanent magnetization: Toward an improved theoretical and experimental foundation, *Earth Planet. Sci. Lett.*, *244*, 515–529.

Ueshima, T., M. Yamamoto, T. Irino, T. Oba, M. Minagawa, H. Narita, and M. Murayama (2006), Paleo-productivity record from core MD01-2421, the mid-latitude western North Pacific, during the last 145,000 years, *Global Planet. Change*, *53*, 21–28.

Usui, Y., T. Shibuya, Y. Sawaki, and T. Komiya (2015), Rock magnetism of tiny exsolved magnetite in plagioclase from a Paleoarchean granitoid in the Pilbara craton, *Geochem. Geophys. Geosyst.*, *16*, 112–125, doi:10.1002/2014GC005508.

Wakabayashi, K., H. Tsunakawa, N. Mochizuki, Y. Yamamoto, and Y. Takigami (2006), Paleomagnetism of the Middle Cretaceous Iritono granite in the Abukuma region, northeast Japan, *Tectonophysics*, *421*, 161–171.

Williams, W., M. E. Evans, and D. Krása (2010), Micromagnetics of paleomagnetically significant mineral grains with complex morphology, *Geochem. Geophys. Geosyst.*, *11*, Q02Z14, doi:10.1029/2009GC002828.

Zhao, X., D. Heslop, and A. P. Roberts (2015), A protocol for variable resolution first-order reversal curve measurements, *Geochem. Geophys. Geosyst.*, *16*, 1364–1377, doi:10.1002/2014GC005680.